Zhang *et al. Satellite Navigation* (2025) 6:26
https://doi.org/10.1186/s43020-025-00179-4

Satellite Navigation
https://satellite-navigation.springeropen.com/

ORIGINAL ARTICLE Open Access

Mitigating ionospheric disturbances impacts on NRTK positioning: an optimization method for adaptive functional and stochastic models

Jinsheng Zhang[1,2], Xiaodong Ren[1*], Yuhang Yang[1], Ahmed Mohamed Elsayed Abdelaziz[1], Xiaohong Zhang[1,3], Guofu Pan[2] and Ke Jiang[2]

Abstract

Currently, solar activity has entered the peak year of its 25th cycle, which is significantly and critically impacting the positioning accuracy and reliability of the Global Navigation Satellite System (GNSS). Intense ionospheric scintillation and fluctuations in Total Electron Content (TEC) can lead to substantial errors in GNSS observations, particularly in low-latitude regions. To address this issue, this study proposed an improved Network Real-Time Kinematic (NRTK) positioning method tailored for complex ionospheric environments. By leveraging the warning information of ionospheric disturbances from the server-end, the proposed method enhances both the accuracy and availability of NRTK positioning with ionospheric residual estimation and adaptive stochastic model at the user-end. Using the data at Hong Kong regional Continuously Operating Reference Station (CORS) from September 2024, we demonstrated that during the high solar activity year, the ionospheric disturbances index Rate Of TEC Index (ROTI) exhibited a strong positive correlation (correlation coefficient: 0.91) with ionospheric interpolation errors on the server-end and a negative correlation (correlation coefficient: − 0.9) with fixing rate on the user-end. Compared to the conventional NRTK method, our approach significantly improves the rover positioning performance. The average fixing rate is increased from 58 to 84%, while the positioning accuracy is improved by 37.6% and 41.6% for the horizontal and vertical components, respectively.

Keywords Global Navigation Satellite System (GNSS), Network Real-Time Kinematic (NRTK), Ionospheric modeling, Ionospheric disturbances, Stochastic model

Introduction

The Global Navigation Satellite Systems (GNSSs) provide users with global, all-weather, and high-precision Positioning, Navigation, and Timing services (PNT) (Gao et al., 2024; Hofmann-Wellenhof et al., 2007). The GNSS regional augmentation technology, based on continuously operating GNSS reference station networks, is a mainstream positioning technique due to its operational convenience, rapid convergence, and high accuracy (Vollath et al., 2002; Wanninger, 2004; Rizos, 2009; Paziewski & Wielgosz, 2014; Weng et al., 2021). These systems, commonly referred to as Network Real-Time Kinematic (RTK) systems, provide error corrections to users using pseudorange and phase observations, enabling real-time centimeter-level positioning services. Network RTK (NRTK) systems typically employ Delaunay triangulation to construct reference station networks and resolve Double-Difference (DD) integer ambiguities between stations in real time (Gao et al., 2002; Zou et al., 2005; Odijk et al.,

*Correspondence:
Xiaodong Ren
xdren@whu.edu.cn
[1] School of Geodesy and Geomatics, Wuhan University, Wuhan 430079, Hubei, China
[2] Guangzhou Hi-Target Navigation Tech Co. Ltd., Guangzhou 511400, Guangdong, China
[3] Chinese Antarctic Center of Surveying and Mapping, Wuhan University, Wuhan 430079, Hubei, China

2010; Li et al., 2014; Zhang et al., 2022; Gu et al., 2024; Liu et al., 2024).

The ionosphere delay is now recognized as one of the dominant error sources in high-precision GNSS positioning. Over the past two decades, extensive research efforts have been devoted to mitigating its impact. Tominaga et al. (2004) investigated the relationship between ionospheric disturbances and carrier-phase positioning errors in mesoscale baselines (approximately 46 km). Their results demonstrated that ambiguity resolution was a challenge on such baselines during specific periods. In the conditions of heightened ionospheric activity or during ionospheric storms, it is particularly difficult for Network RTK (NRTK) users to achieve fixed solutions (Luo et al., 2005; Wielgosz et al., 2005; Gianniou et al., 2012; Dobelis et al., 2017; Paziewski et al., 2022). This challenge is exacerbated in low-latitude regions, where positioning accuracy degrades significantly when the distance between reference stations exceeds 30 km (Charoenkalunyuta et al., 2012). Bae et al. (2018) assessed the performance of NRTK in navigation applications, concluding that even low-cost receivers, when paired with high-quality GNSS antennas, can achieve positioning accuracy and stability comparable to geodetic-grade equipment in dynamic conditions. Odolinski et al. (2019) evaluated the performance of smartphones and low-cost multi-GNSS single- and dual-frequency RTK devices at varying levels of ionospheric disturbance (low, medium, and high). Follestad et al. (2021) revealed that the impact of the ionosphere on GPS-RTK performance exhibited strong seasonal and diurnal variations. The recent studies by Dutta et al. (2022) and Zhang et al. (2024) have demonstrated that during the periods of peak ionospheric activity, frequent cycle slips may occur on multiple satellites, potentially causing RTK solutions to remain in float status and leading to a degradation in the accuracy of fixed solutions.

Overall, the poor NRTK positioning performance during ionospheric disturbances is mainly caused by the low accuracy of ionospheric interpolation and the lack of ionospheric interpolation precision information. The ionospheric and tropospheric errors between rover stations and reference stations are corrected with an interpolation method on server-end (Cui et al., 2018; Gao et al., 2025; Gong, 2008; Gu et al., 2022; Mei, 2008; Mirmohammadian et al., 2022; Yang et al., 2021). Wanninger (1995) first proposed the Linear Interpolation Model (LIM), which uses the horizontal coordinates of reference stations as parameters to establish an interpolation surface. To improve the accuracy of ionospheric interpolation models, numerous researchers have conducted in-depth studies and proposed various approaches, such as Linear Combination Model (LCM), Low-order Surface Model (LSM) and Distance-dependent Interpolation Model (DIM). (Han, 1996; Wübbena et al., 1996; Han et al., 1997; Gao et al., 1997; Raquet, 1998; Gao et al., 1998; Fotopoulos et al., 2001; Gao et al., 2025). Comparisons of these interpolation methods are reported in multiple studies (Fotopoulos et al., 2001; Dai et al., 2003; Al-Shaery et al., 2011; Tang et al., 2016), demonstrating that these methods exhibit a good modeling performance during the ionospheric quiet period. Accordingly, in conventional NRTK positioning, the residual ionospheric delays are usually not considered in DD observation model (Wu, 2009; Zhang et al., 2024). However, solar activity has now entered the peak year of its 25th cycle, leading to strong enhanced ionospheric disturbances (Jha et al., 2024). The existing ionospheric modeling methods experience precision degradation during the period of ionospheric activity (Charoenkalunyuta et al., 2014; Liu et al., 2020; Zhang et al., 2025), which leads to large ionospheric modeling residuals and consequently degrades the accuracy, availability, and continuity of NRTK services (Odolinski et al., 2019; Follestad et al., 2021; Peng et al., 2021; Dutta et al., 2022; Zhang et al., 2024). Consequently, achieving centimeter-level accuracy with NRTK positioning still remains a challenge during ionospheric activity period.

In order to mitigate the influence of the ionospheric interpolation residuals, the ionosphere-weighted model was proposed (Odijk et al., 2000; Julien et al., 2004; Wielgosz et al., 2005; Wielgosz, 2011; Odolinski et al., 2017; Mi et al., 2019; Gao et al., 2022). This method has significantly advanced the medium- to long-baseline RTK positioning (Paziewski, 2016; Wang et al., 2023; Zhu et al., 2023). Currently, integrating multi-station network ionospheric corrections with ionosphere-weighted models has emerged as one of the most effective strategies for precise GNSS relative positioning. Paziewski and Sieradzki (2020) proposed an improved method that utilizes the correction rate of Total Electron Content (TEC) to mitigate the effects of dynamic spatiotemporal TEC variations during ionospheric disturbances. Using the data from August 25 and 26 in 2018, they demonstrated that their new method achieved an improvement of 20% in ambiguity fixing success rate compared to both the ionosphere-float model and the ionosphere-weighted model. Despite the ongoing advancements, ionospheric parameter estimation methods continue to encounter difficulties under strong ionospheric disturbances, particularly in the initialization of ionospheric parameters, the specification of suitable process noise, and the formulation of an appropriate observation stochastic model.

In this contribution, we proposed an improved NRTK positioning method optimized for challenging ionospheric environments. By employing ionospheric disturbances information broadcast on server-end, the

ionospheric parameters estimation is dynamically activated on user-end and the process noise of ionosphere parameter is adaptively adjusted. In addition, the disturbance information is used to refine the stochastic model of phase and code observations. We demonstrate that the availability and accuracy of RTK positioning are significantly enhanced in severe ionospheric disturbance conditions by mitigating the residual errors introduced by the ionospheric interpolation model on server-end.

Methodology

Conventional NRTK method on server-end and user-end

Server-end baseline resolution and atmospheric interpolation

The NRTK baseline solution employs DD observation model. Given the precisely known coordinates of the reference stations, the DD observation equations are formulated as follows:

$$\begin{cases} \Delta\nabla P_{r,b}^{(i,j)} = \Delta\nabla\rho_{r,b}^{(i,j)} + \Delta\nabla I_{r,b}^{(i,j)} + \Delta\nabla T_{r,b}^{(i,j)} + \varepsilon_{\Delta\nabla_P} \\ \lambda\Delta\nabla\varphi_{r,b}^{(i,j)} = \Delta\nabla\rho_{r,b}^{(i,j)} - \Delta\nabla I_{r,b}^{(i,j)} + \Delta\nabla T_{r,b}^{(i,j)} - \lambda\Delta\nabla N_{r,b}^{(i,j)} + \varepsilon_{\Delta\nabla_\varphi} \end{cases} \quad (1)$$

where $\Delta\nabla$ represents DD between stations and satellites, P represents the pseudorange observation, φ represents the carrier phase observation, i and j denote satellites, r stands for the rover station, and b denotes the reference station, ρ is the satellite-to-receiver range, I stands for ionospheric delay error, T is the tropospheric delay error, λ is the carrier phase wavelength, N represents the integer carrier phase ambiguity, and $\varepsilon_{\Delta\nabla_P}$ and $\varepsilon_{\Delta\nabla_\varphi}$ represent the noise of pseudorange and carrier phase observations, respectively.

In the triangular network diagram shown in Fig. 1, A, B, and C represent reference stations, U denotes the actual user station, and V indicates the location where virtual observations are generated near the user station. After resolving the DD ambiguities of the three baselines (AB, BC, CA) using Eq. (1), DD tropospheric and ionospheric delays along these baselines can be determined precisely. Based on the principles of triangulation-based interpolation, the tropospheric and ionospheric delays near the user station can be interpolated.

Generation of VRS phase observations

In the process of generating phase observations at a Virtual Reference Station (VRS), the first step is to compute single differences for the observations between the master station (the nearest reference station to VRS) and the VRS, yielding (Herbert et al., 2002; Li, 2007):

$$\begin{cases} \Delta P_{A,V}^{(i)} = \Delta\rho_{A,V}^{(i)} + \Delta I_{A,V}^{(i)} + \Delta T_{A,V}^{(i)} + c\Delta t_{A,V} + \varepsilon_{\Delta_P} \\ \lambda\Delta\varphi_{A,V}^{(i)} = \Delta\rho_{A,V}^{(i)} - \Delta I_{A,V}^{(i)} + \Delta T_{A,V}^{(i)} - \lambda\Delta N_{A,V}^{(i)} + c\Delta t_{A,V} + \varepsilon_{\Delta\varphi} \end{cases} \quad (2)$$

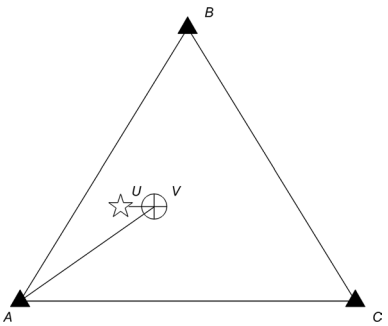

Fig. 1 The schematic diagram of a triangulation network

where $\Delta t_{A,V} = t_A - t_V$ represents the single-difference receiver clock bias between the master station and the VRS, and $\Delta N_{A,V}^{(i)} = N_A^i - N_V^i$ denotes the single-difference ambiguity between the master station and the VRS.

By moving the master station observations to the right side of the equation, Eq. (2) can be reformulated as:

$$\begin{cases} P_V^{(i)} = P_A^{(i)} + \Delta\rho_{A,V}^{(i)} + \left(\Delta I_{A,V}^{(j)} + \Delta\nabla I_{A,V}^{(j,i)}\right) \\ + \left(\Delta T_{A,V}^{(j)} + \Delta\nabla T_{A,V}^{(j,i)}\right) + c\Delta t_{A,V} + \varepsilon_{\Delta P} \\ \lambda\varphi_V^{(i)} = \lambda\varphi_A^{(i)} + \Delta\rho_{A,V}^{(i)} - \left(\Delta I_{A,V}^{(j)} + \Delta\nabla I_{A,V}^{(j,i)}\right) \\ + \left(\Delta T_{A,V}^{(j)} + \Delta\nabla T_{A,V}^{(j,i)}\right) - \lambda\Delta N_{A,V}^{(i)} + c\Delta t_{A,V} + \varepsilon_{\Delta\varphi} \end{cases} \quad (3)$$

where the superscript j denotes the reference satellite. At each epoch, the terms $\Delta I_{A,V}^{(j)}$, $\Delta T_{A,V}^{(j)}$ and $c\Delta t_{A,V}$ can be eliminated in the subsequent user-side RTK DD algorithms. Additionally, since the ambiguity N_V^i at the VRS can be set to zero, the complete mathematical expression for the undifferenced VRS observations are:

$$\begin{cases} P_V^{(i)} = P_A^{(i)} + \Delta\rho_{A,V}^{(i)} + \Delta\nabla I_{A,V}^{(i,j)} + \Delta\nabla T_{A,V}^{(i,j)} + \varepsilon_{\Delta P} \\ \varphi_V^{(i)} = \varphi_A^{(i)} + \Delta\rho_{A,V}^{(i)}/\lambda - \Delta\nabla I_{A,V}^{(i,j)}/\lambda + \Delta\nabla T_{A,V}^{(i,j)}/\lambda + \varepsilon_{\Delta\varphi} \end{cases} \quad (4)$$

By forming an ultra-short baseline between the VRS and the rover station, the ambiguity parameters can be rapidly resolved (Teunissen, 1995), which enables rapid centimeter-level positioning solutions.

Improved NRTK method on server-end and user-end

In conventional NRTK method, the residuals of DD ionospheric and tropospheric delays are typically neglected. However, during the periods of intense ionospheric disturbances, the residual ionospheric delays become the dominant source of positioning errors. To address this issue, our study adaptively determines whether to estimate ionospheric parameters based on the level of ionospheric activity, utilizing the ionospheric disturbances index provided on server-end of NRTK.

Computation of ionospheric disturbance information on server-end

This study adaptively adjusts both the user-end functional model and stochastic model based on ionospheric disturbance information provided on server-end. The ionospheric disturbance indices are defined by the following formulas (Pi et al., 1997; Ren et al., 2024):

$$r = \frac{S(t+\triangle t) - S(t)}{\triangle t} \tag{5}$$

where t represents epoch time; $\triangle t$ represents the duration of ionospheric temporal variation; S represents the slant TEC along the signal propagation path; and r represents the change rate of STEC during Δt. Then, the Rate Of TEC Index (ROTI) can be calculated as follows (Pi et al., 1997; Ren et al., 2024):

$$R = \sqrt{\langle r^2 \rangle - \langle r \rangle^2} \tag{6}$$

where R represents ROTI; < > represents the average value over a time interval.

In this study, ROT is calculated using the data sampled at 30-s intervals, whereas ROTI is computed over a 5-min time window (Jia et al., 2024; Pi et al., 1997).

Refinement of the user-end functional model

Based on the ionospheric disturbance information provided on server-end of NRTK, the user-end functional model requires corresponding refinements. The new functional model is established by extending the conventional DD RTK functional model with ionospheric residual parameters, expressed as:

$$\begin{cases} \Delta\nabla P_{k,U,V}^{(i,j)} = \Delta\nabla\rho_{k,U,V}^{(i,j)} + \Delta\nabla I_{k,U,V}^{(i,j)} + \varepsilon_{\Delta\nabla_P} \\ \Delta\nabla L_{k,U,V}^{(i,j)} = \Delta\nabla\rho_{k,U,V}^{(i,j)} - \Delta\nabla I_{k,U,V}^{(i,j)} - \lambda\Delta\nabla N_{k,U,V}^{(i,j)} + \varepsilon_{\Delta\nabla_\varphi} \end{cases} \tag{7}$$

Assuming there are $m+1$ common visible satellites at the VRS and the rover station, the DD observation equation from Eq. (7) can be written in matrix form as follows:

$$\boldsymbol{Y} = \begin{pmatrix} \boldsymbol{Y_P} \\ \boldsymbol{Y_L} \end{pmatrix} \tag{8}$$

where $\boldsymbol{Y_P} = \left(\Delta\nabla P_{1,U,V}^{(1,j)}, \Delta\nabla P_{2,U,V}^{(1,j)}, \ldots, \Delta\nabla P_{1,U,V}^{(m,j)}, \Delta\nabla P_{2,U,V}^{(m,j)}\right)^{\mathrm{T}}$, $\boldsymbol{Y_L} = \left(\Delta\nabla L_{1,U,V}^{(1,j)}, \Delta\nabla L_{2,U,V}^{(1,j)}, \ldots, \Delta\nabla L_{1,U,V}^{(m,j)}, \Delta\nabla L_{2,U,V}^{(m,j)}\right)^{\mathrm{T}}$.

Therefore, the parameters to be estimated are listed as follows:

$$\boldsymbol{X} = \left(X_{\mathrm{pos}}\ X_{\mathrm{ion}}\ X_{\mathrm{amb}}\right)^{\mathrm{T}} \tag{9}$$

where $\boldsymbol{X_{pos}} = \left(x_{U,V}\ y_{U,V}\ z_{U,V}\right)$, $\boldsymbol{X_{ion}} = \left(\Delta\nabla I_{1,U,V}^{(1,j)} \cdots \Delta\nabla I_{1,U,V}^{(m,j)}\right)$ $\boldsymbol{X_{ion}} = \left(\Delta\nabla I_{1,U,V}^{(1,j)} \cdots \Delta\nabla I_{1,U,V}^{(m,j)}\right)$, $\boldsymbol{X_{amb}} = \left(\Delta\nabla N_{1,U,V}^{(1,j)}\ \Delta\nabla N_{2,U,V}^{(1,j)} \cdots \Delta\nabla N_{1,U,V}^{(m,j)}\ \Delta\nabla N_{2,U,V}^{(m,j)}\right)$。

The stochastic model of the observations after DD is given by Eq. (10):

$$\boldsymbol{D} = \begin{pmatrix} \boldsymbol{T}\boldsymbol{D}_{\mathrm{SD}}^{\mathrm{P}}\boldsymbol{T}^{\mathrm{T}} & \\ & \boldsymbol{T}\boldsymbol{D}_{\mathrm{SD}}^{\mathrm{L}}\boldsymbol{T}^{\mathrm{T}} \end{pmatrix} \tag{10}$$

The matrix $\boldsymbol{T}$ denotes the transformation matrix from single-difference to DD observations, where the column with a value of -1 corresponds to the reference satellite:

$$\boldsymbol{T} = \begin{pmatrix} 1 & & -1 & & \\ 1 & & -1 & & \\ & 1 & -1 & & \\ & 1 & -1 & & \\ & \cdots & \vdots & \cdots & \\ & & -1 & 1 & \\ & & -1 & 1 & \\ & & -1 & & 1 \\ & & -1 & & 1 \end{pmatrix}_{2(m-1),2m} \tag{11}$$

The variance–covariance matrices of pseudorange and phase single-difference observations are given by Eq. (12) and Eq. (13). σ^2 and η^2 denote the variances of the undifferenced pseudorange and carrier phase observations, respectively, where the subscripts denote the satellite frequency, station, and satellite, respectively, in sequential order:

$$\boldsymbol{D}_{\mathrm{P,SD}} = \begin{pmatrix} \sigma_{1,U,1}^2 + \sigma_{1,V,1}^2 & & & & \\ & \sigma_{2,U,1}^2 + \sigma_{2,V,1}^2 & & & \\ & & \ddots & & \\ & & & \sigma_{1,U,m}^2 + \sigma_{1,V,m}^2 & \\ & & & & \sigma_{2,U,m}^2 + \sigma_{2,V,m}^2 \end{pmatrix}_{2m,2m} \tag{12}$$

$$\boldsymbol{D}_{\mathrm{L,SD}} = \begin{pmatrix} \eta_{1,U,1}^2 + \eta_{1,V,1}^2 & & & & \\ & \eta_{2,U,1}^2 + \eta_{2,V,1}^2 & & & \\ & & \ddots & & \\ & & & \eta_{1,U,m}^2 + \eta_{1,V,m}^2 & \\ & & & & \eta_{2,U,m}^2 + \eta_{2,V,m}^2 \end{pmatrix}_{2m,2m} \tag{13}$$

In kinematic GNSS positioning, a discretized Kalman filtering model is often employed, with the linearized equations as follows:

$$\begin{cases} \boldsymbol{V}_k = \boldsymbol{A}_k \hat{\boldsymbol{X}}_k - \boldsymbol{Y}_k \\ \overline{\boldsymbol{X}}_k = \boldsymbol{\Phi}_{k,k-1} \hat{\boldsymbol{X}}_{k-1} + W_k \end{cases} \tag{14}$$

where $\boldsymbol{A}_k$ denotes the observation design matrix; $\boldsymbol{Y}_k$ represents DD observation vector at time t_k; $\overline{\boldsymbol{X}}_k$ is the predicted state vector; $\hat{\boldsymbol{X}}_k$ and $\hat{\boldsymbol{X}}_{k-1}$ are the estimated values at times t_k and t_{k-1}, respectively; $\boldsymbol{\Phi}_{k,k-1}$ denotes the state transition matrix; and $\boldsymbol{W_k}$ is process noise; The covariance matrix $\overline{\boldsymbol{X}}_k$ is given by the following equation:

$$\boldsymbol{\Sigma}_{\overline{X}_k} = \boldsymbol{\Phi}_{k,k-1} \boldsymbol{\Sigma}_{\hat{X}_{k-1}} \boldsymbol{\Phi}_{k,k-1}^{\mathrm{T}} + \boldsymbol{\Sigma}_{W_k} \tag{15}$$

where $\boldsymbol{\Sigma}_{\hat{\boldsymbol{X}}_{\boldsymbol{k-1}}}$ is variance of the estimated value, and $\boldsymbol{\Sigma}_{\boldsymbol{W_k}}$ represents the process noise. In contrast to high-dynamic scenarios such as aircraft and vehicles, most situations encountered during NRTK user operations are low-dynamic walking modes. Furthermore, considering data sampling interval of 1 s in this study, only positional changes are taken into account in state prediction, omitting estimation of velocity and acceleration-related parameters (Takasu et al., 2009). The specific form is shown in Eq. (16):

$$\begin{cases} \overline{X}_{k,\mathrm{pos}} = \hat{X}_{k,\mathrm{spp}} \\ \overline{X}_{k,\mathrm{ion}} = \hat{X}_{k-1,\mathrm{ion}} \\ \overline{X}_{k,\mathrm{amb}} = \hat{X}_{k-1,\mathrm{amb}} \end{cases} \tag{16}$$

where $\hat{X}_{k,\mathrm{spp}}$ denotes the estimated parameters of standard point positioning coordinates at time t_k, $\hat{X}_{k-1,\mathrm{ion}}$ represents the filtered estimates of ionosphere parameters at time t_{k-1}, $\hat{X}_{k-1,\mathrm{amb}}$ represents the filtered estimates of ambiguity parameters at time t_{k-1}. and the covariance of $\boldsymbol{W}_k$ is expressed by Eq. (17):

$$\boldsymbol{\Sigma}_{W_k} = \begin{pmatrix} \boldsymbol{\Sigma}_{W_{k,\mathrm{spp}}} & & \\ & \Sigma_{W_{k,\mathrm{ion}}} & \\ & & \Sigma_{W_{k,\mathrm{amb}}} \end{pmatrix}_{3m+3,3m+3} \tag{17}$$

where $\boldsymbol{\Sigma}_{W_{k,\mathrm{spp}}}$ represents the process noise matrix of position in each direction having a value of 10^2; $\Sigma_{W_{k,\mathrm{amb}}}$ represents the the process noise matrix of ambiguity with a value of $(10^{-4})^2$ (Takasu et al., 2009); and $\Sigma_{W_{k,\mathrm{ion}}}$ denotes the process noise variance of the ionospheric parameters.

In previous studies, the process noise of the ionospheric parameters was typically set as empirical constants. However, during periods of elevated solar activity, the ionosphere exhibits highly dynamic behavior, rendering such empirical constants inadequate. This inadequacy is particularly pronounced during ionospheric scintillation events, where the constants are unable to reflect the rapid epoch-to-epoch fluctuations in ionospheric delays. To overcome this limitation, an approach is proposed in which the fixed process noise parameters are replaced by real-time, epoch-wise ionospheric delay variations derived from geometry-free (GF) combination observations. Equation (18) provides DD GF observations:

$$\Delta\nabla L_{\mathrm{GF}}^{(i,j,U,V)} = \Delta\nabla L_2^{(i,j,U,V)} - \Delta\nabla L_1^{(i,j,U,V)} = \alpha \cdot \Delta\nabla I_1^{(i,j,U,V)} + B + \varepsilon_{\Delta\nabla_L} \tag{18}$$

where $\Delta\nabla L_{\mathrm{GF}}^{(i,j,U,V)}$ represents the double difference GF observations, $\alpha = \frac{f_2^2 - f_1^2}{f_2^2}$ and $B = \lambda_1 \Delta\nabla N_1 - \lambda_2 \Delta\nabla N_2$ represents the ambiguity term, and $\varepsilon_{\Delta\nabla_L}$ is observation noise. According to formula (18), the calculation formula for DD ionosphere delays is:

$$\Delta\nabla I_1^{(i,j,U,V)} = \left(\Delta\nabla L_{\mathrm{GF}}^{(i,j,U,V)} - B\right)/\alpha \tag{19}$$

When no cycle slips occur, the ambiguity terms B remain constant and can be eliminated by epoch differencing. Therefore, the process noise variance of the ionospheric parameters $\Sigma_{W_{k,\mathrm{ion}}}$ is derived based on the ionospheric delay variations between epochs t_{k-1} and t_k:

$$\begin{aligned} \Sigma_{W_{k,ion}} &= \left(\Delta\nabla I_{t_k,1}^{(i,j,U,V)} - \Delta\nabla I_{t_{k-1},1}^{(i,j,U,V)}\right)^2 \\ &= \left(\left(\Delta\nabla L_{t_k,\mathrm{GF}}^{(i,j,U,V)} - \Delta\nabla L_{t_{k-1},\mathrm{GF}}^{(i,j,U,V)}\right)/\alpha\right)^2 \end{aligned} \tag{20}$$

According to Eq. (20) and the ionospheric disturbance index provided on server-end, the user-end assesses the occurrence of rapid changes in ionospheric gradients. When such variations are detected, the process noise associated with ionospheric parameter estimation is dynamically modified.

Construction of the user-end stochastic model

During the periods of intense ionospheric disturbances, a substantial proportion of satellites are affected by ionospheric scintillation, resulting in significant degradation in both ambiguity resolution success rate and positioning accuracy. To address this issue, this study develops an improved stochastic model for user-end RTK positioning, incorporating ionospheric delay residual estimation and a quantitative analysis of the correlation between ROTI and ambiguity fixing rate. When the intensity of scintillation affecting satellite signals exceeds predefined thresholds, the system applies piece-wise linear functions to reduce the weights of virtual observations from the impacted satellites. This strategy effectively mitigates the influence of virtual observations with large ionospheric interpolation errors on RTK positioning performance.

The specific implementation process is as follows.

Firstly, the average ROTI for each satellite over a period is calculated as:

$$\overline{R}_s = \frac{1}{N}\sum_{i=1}^{N} R_i \tag{21}$$

where N denotes the number of ROTI for satellite s within the period, and $\overline{R}_s$ is the average ROTI for satellite s.

Secondly, the average ROTI are sorted in descending order as $\overline{R}_1, \overline{R}_2, \ldots, \overline{R}_M$. By excluding the top $k (k = 0, 1, \ldots, M-1)$ satellites, the ionospheric scintillation proportion for the remaining $M-k$ satellites is calculated as:

$$S_k = \frac{1}{M-k}\sum_{i=k+1}^{M} g_i \tag{22}$$

According to Pereira et al. (2021), ionospheric scintillation occurs when ROTI exceeds 0.2 Total Electron Content Unit (TECU) every minute. Here, g_i equals 1 if $\overline{R}_s$ exceeds 0.2, otherwise 0. S_k represents the scintillation proportion after excluding the top k satellites.

Finally, the weight of virtual observations W_k is determined by considering both the scintillation proportion S_k and ionospheric interpolation error ε_k:

$$W_k = \begin{cases} 0, & S_k > b \\ W_{\text{elev}}(e_k) \cdot \left(\frac{c}{f(S_k, \varepsilon_k)}\right)^2, & a < S_k \le b \\ W_{\text{elev}}(e_k) \cdot 1, & S_k \le a \end{cases} \tag{23}$$

where $W_{\text{elev}}(e_k) = \frac{\sigma_0^2}{\sigma^2}$, e_k represents satellite elevation, σ_0^2 denotes the unit weight variance, σ^2 is observation variance modeled as a simplified function of the elevation angle (Dai et al., 2017), $f(S_k, \epsilon_k)$ represents the joint influence function of scintillation proportion and interpolation error (detailed later), c represents the coefficient related to interpolation error, and a and b correspond to the down weighting and exclusion threshold, respectively. Multiple factors including ionospheric characteristics and the quality of observation data should be comprehensively evaluated for the determination of these scenario-adaptive thresholds.

Figure 2 illustrates the workflow of the proposed NRTK on server-end and user-end algorithms during ionospheric scintillation periods:

Table 1 presents a comparative analysis between conventional NRTK user-end RTK method and the proposed user-end method under active ionospheric conditions. In conventional network RTK user-end method, the impacts of ionospheric and tropospheric interpolation residuals are generally neglected and observation weighting primarily uses elevation-dependent models. However, during the periods of intense solar activity and severe ionospheric disturbances, ionospheric interpolation residuals increase significantly and cannot be directly ignored. To address the defect of conventional RTK method that overlooks ionospheric interpolation errors on user-end, we propose a novel RTK positioning method combining service-end ionospheric disturbance information generation and user-end ionospheric interpolation residual estimation (denoted as Method A, see Table 1). By integrating ROTI with elevation-dependent weighting models, we further optimize the stochastic model for user-end RTK positioning, enhancing adaptability of algorithms across diverse for ionospheric environments (denoted as Method B, see Table 1).

Results and analysis

To mitigate the increaseing ionospheric disturbances during the peak of Solar Cycle 25, major NRTK service providers have densified their reference stations in low-latitude regions of China, reducing inter-station distances to less than 30 km. Although such a dense reference stations are employed, NRTK positioning performance remains unstable and unreliable during the periods of heightened ionospheric activity. Therefore, the data from a reference network with inter-station distances of less than 30 km were employed in this study. The network is in the low-latitude Hong Kong (HK) region (114° E–114.5 °E, 22.15 °N–22.55 °N). Four Continuously Operating Reference Stations (CORS) within the study area—HKKT, HKOH, HKST, and HKWS—were selected for analysis. Their spatial distribution is shown in Fig. 3, where triangular symbols represent the reference stations, and the red dot indicates the location of the rover station. The VRS represented by the red dot, is generated at the same location of the rover station. The rover station HKST is approximately 16 km away from the nearest

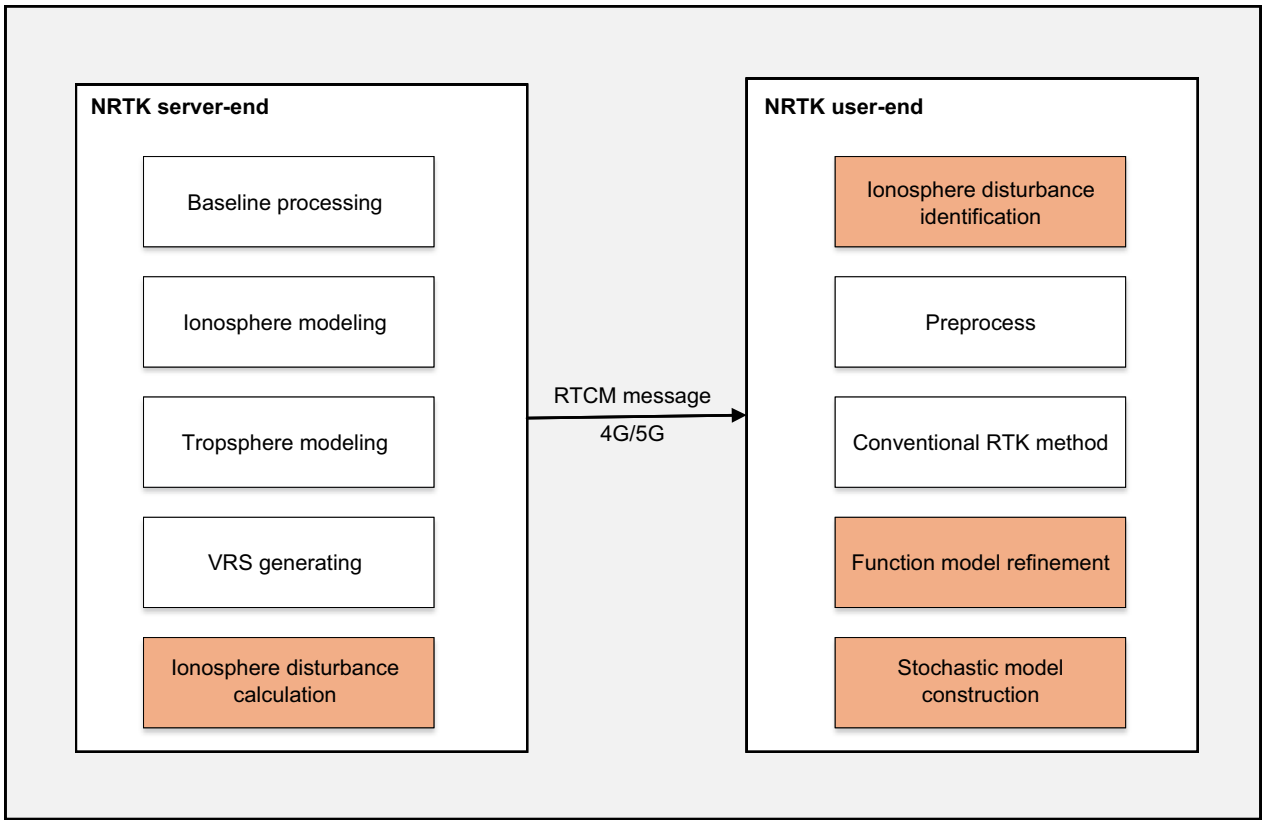

Fig. 2 Diagram of NRTK on server-end and user-end method

Table 1 Comparison of three NRTK user-end method strategies

Items	Convention RTK method	Method A	Method B
DD ionosphere residual	Ignore	Adaptive parameter estimation	Adaptive parameter estimation
DD troposphere residual	Ignore	Ignore	Ignore
Stochastic model	Elevation-dependent model	Elevation-dependent model; adaptive determination of ionospheric process noise	Elevation-dependent model; adaptive determination of ionospheric process noise; construction stochastic model with ROTI

reference station, HKKT, which is the master station in the network.

The observations in January and September of 2019 (a year of low solar activity) and 2024 (a year of high solar activity) are selected. Figure 4 displays the 68th, 95th, and 99th percentile values of the daily ROTI. The results reveal that even the 99th percentile ROTI values in 2019 remained stable, where its values in 2024 show frequent spikes, with more pronounced fluctuations in September than January. This indicates frequent occurrences of intense ionospheric scintillation in September 2024. Because ionospheric scintillation exhibits distinct seasonal characteristics, typically occurring more frequently during the vernal and autumnal equinoxes (Liu et al., 2015). Figure 5 presents the Vertical Total Electron Content (VTEC) time series at HKST station for January and September of 2019 and 2024. The VTEC values are derived with interpolation using ionospheric grid files (ftp://igs.gnsswhu.cn/pub/gps/products/ionex) released by the International GNSS Service (IGS). Notably, the peak VTEC values in 2024 reached approximately 3–4 times of those observed in 2019, indicating a significant enhancement in ionospheric activity during the solar active period.

Figure 6 presents heatmap distributions of the ambiguity fixing rate at the rover station for January and September of both 2019 and 2024. The horizontal axis represents GPS time, and the vertical axis indicates calendar dates,

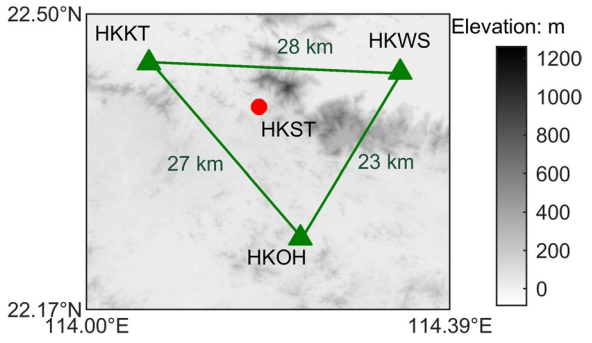

Fig. 3 Hong Kong triangle network stations map (Zhang et al., 2024)

with each cell showing the hourly fixing rate for a given day. In this study, a fixed solution is defined as one with horizontal positioning errors less than 10 cm and vertical errors less than 20 cm. For the evaluation of result accuracy, the reference coordinates of the HKST station were obtained from the official website of the HK Geodetic Survey (https://www.geodetic.gov.hk/common/data/pdf/SatRef_Coord.pdf). The color bar on the right reflects the fixing rate, with values increasing from red (low) to green (high).The heatmaps show substantial fluctuations in the fixing rate during September 2024, particularly after GPS time 12:00, which corresponds to 20:00 local time in HK (UTC+8). Specifically, the average fixing rates in January 2019, September 2019, January 2024, and September 2024 are 99.78%, 99.98%, 99.97%, and 93.19%, with the number of periods in which the fixing rate exceeding 90% being 715, 720, 720, and 629, respectively. Notably, in September 2024, the average fixing rate between GPS time 12:00 and 24:00 is 86.52%.

A comparison with Fig. 4 indicates that the dates with significant variability in fixing rates are closely associated with frequent ionospheric scintillation events. In contrast, the fixing rate remains consistently high throughout the day during the periods of calm ionospheric conditions without scintillation. Since virtual observations are generated by interpolating atmospheric values of reference stations, their accuracy is directly influenced by the quality of atmospheric interpolation. During the period of onospheric disturbances, the increase in interpolation errors reduces the reliability of virtual observations, resulting in lower fixing rates during affected periods.

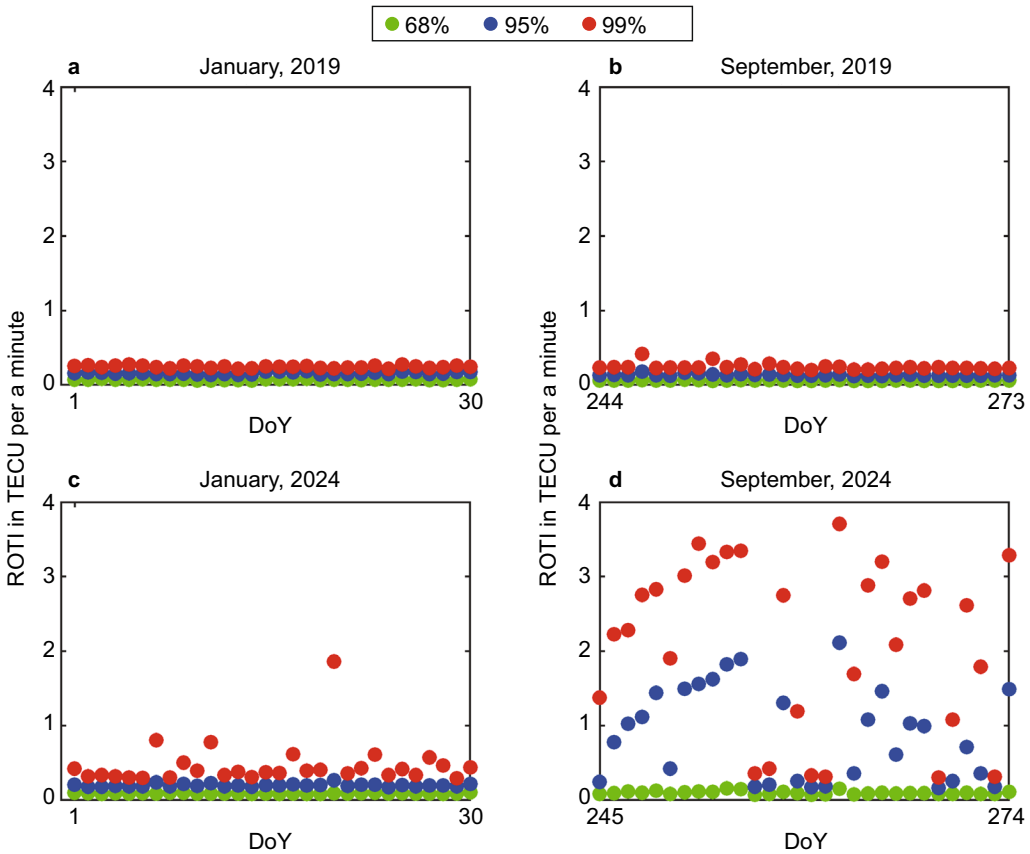

Fig. 4 68th, 95th, and 99th percentile values of ROTI in January and September of 2019 and 2024

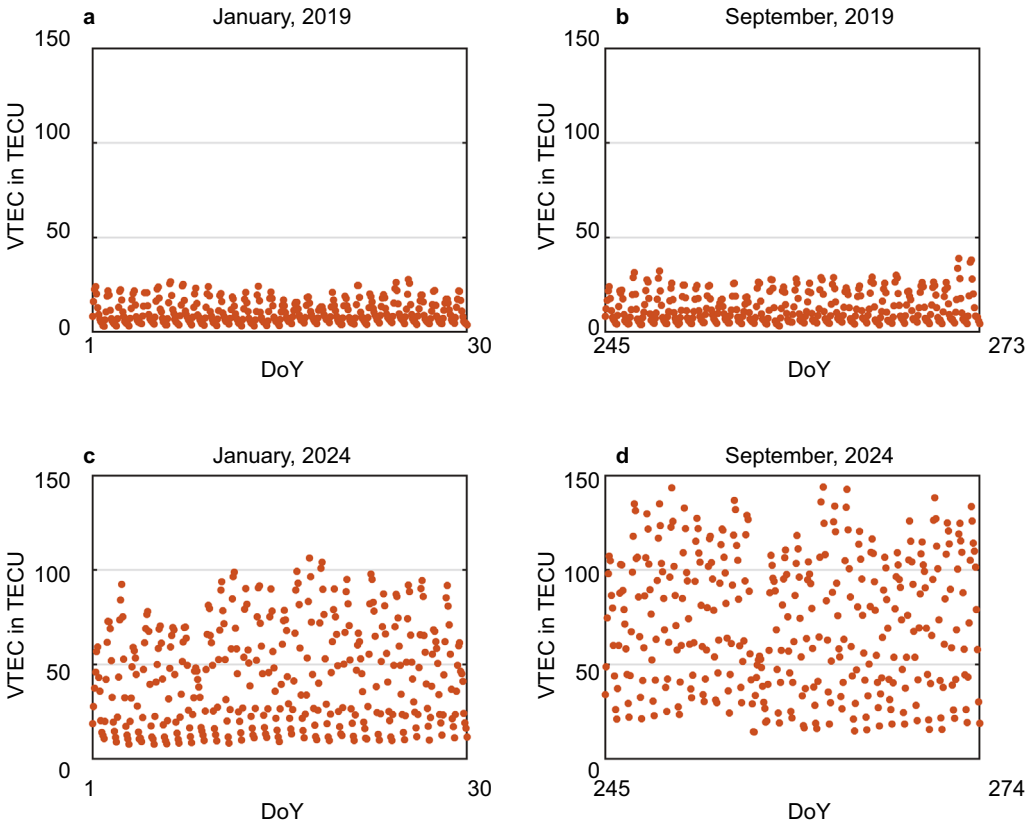

Fig. 5 VTEC time series of the ionosphere in January and September of 2019 and 2024

To further investigate the relationships among atmospheric interpolation accuracy, ROTI, and ambiguity fixing rate, this study presents graphical analyses illustrating the correlation between the proportion of ionospheric scintillation and ionospheric interpolation errors, as well as the correlation between scintillation proportion and user-end fixing rate. The ROTI values were calculated using the data sampled at 30-s intervals with a 5-min computation window. A satellite is considered to be affected by scintillation when its ROTI exceeds 0.2 TECU/min.

In Fig. 7, the horizontal axis represents the average Root Mean Square (RMS) of ionospheric interpolation errors for all satellites per hour, while the vertical axis denotes the hourly percentage of satellites affected by scintillation. The average RMS interpolation error is computed as follows: first, DD ionospheric delays are derived from the HKKT–HKST baseline to serve as reference values. Then, using the NRTK ionospheric interpolation model, the DD ionospheric delay between HKKT (master station) and HKST (rover station) is interpolated. The interpolation error is obtained by subtracting the reference value from the model-derived value. The RMS error is calculated for each satellite, and the hourly average is computed for all satellites. Figure 7 shows that in 2024, a year of high solar activity, low levels of ionospheric scintillation (below 30%) correspond to small interpolation errors (RMS below 10 cm). As the proportion of the satellites whose signals are affected by scintillation increases, the interpolation errors also rise. For instance, when the proportion exceeds 50%, the interpolation error RMS reaches or exceeds 20 cm. The correlation coefficient between the proportion of scintillation and interpolation error in 2024 is 0.91, indicating a strong positive correlation (Cohen, 1988). In contrast, the same correlation in 2019, a year of low solar activity, is only 0.11, suggesting a weak relationship.

However, in real-time applications, the true ionospheric interpolation error is not directly observable. By conducting a rigorous correlation analysis between the proportion of ionospheric scintillation and ionospheric interpolation errors in 2024, a quantitative functional relationship can be established. This relationship provides a foundation for enhancing the stochastic modeling of virtual observation errors in network RTK user-end processing. In this study, a linear regression analysis was applied to the experimental dataset to model the correlation between scintillation proportion and interpolation

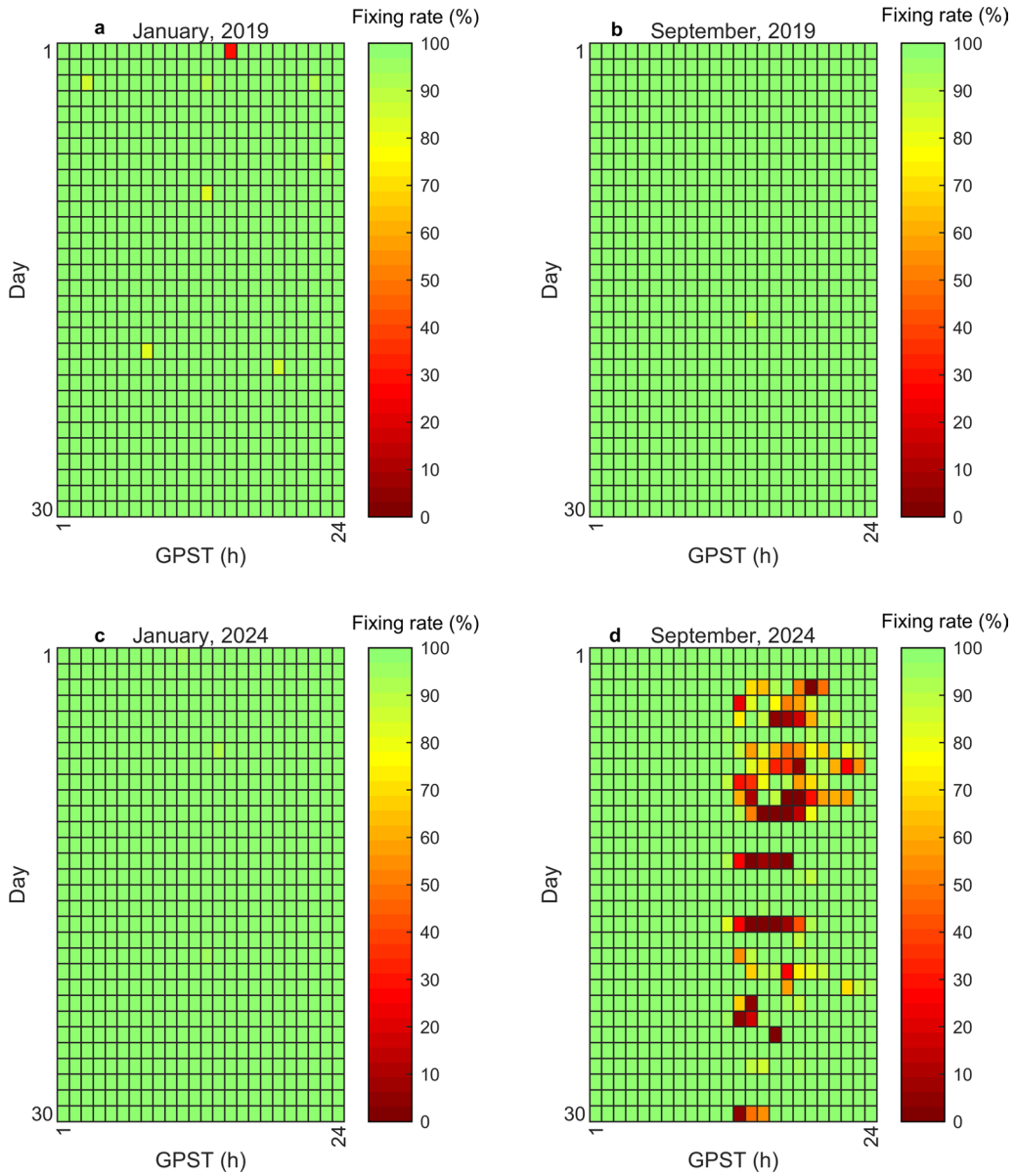

Fig. 6 Fixing rate heatmap of conventional RTK method in NRTK mode

residuals, resulting in a statistically derived empirical equation:

$$\varepsilon = 0.31S + 0.20 \tag{24}$$

where S represents the proportion of ionospheric scintillation measured in percentage and ε is the corresponding ionospheric interpolation error measured in centimeters.

As illustrated in Fig. 7, in quiet ionospheric conditions, the RMS of ionospheric interpolation error remains within 5 cm. By integrating Eqs. (22) and (23), the stochastic model for virtual observations can be further refined by jointly considering both elevation-dependent weighting and ionospheric activity levels. For instance, when the proportion reaches 40%, the corresponding interpolation error estimated from Eq. (24) is 12.6 cm. Compared to the nominal interpolation error of 5 cm in quiet conditions, the observation variance should be scaled by a factor of $(12.6/5)^2$ based on the elevation-dependent model. As a result, the corresponding observation weight is reduced to approximately one-sixth (1/6.35) of its original value.

As shown in the right panel of Fig. 8, in the year 2024, when the proportion of satellites affected by ionospheric scintillation is low (below 20%), the user-end

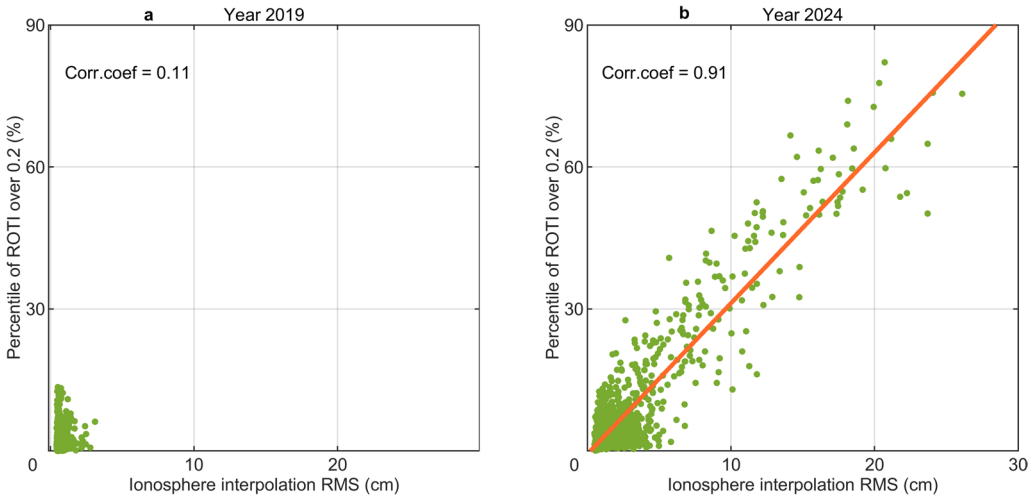

Fig. 7 Relationship between the proportion of ionospheric scintillation and the ionospheric interpolation error

ambiguity fixing rate generally remains high, often approaching or reaching 100%. As the proportion gradually increases, the fixing rate exhibits a notable downward trend. Specifically, when the proportion of satellites with ROTI values exceeding 0.2 TECU/min reached 40% to 60%, the fixing rate declines to approximately 50–70%. The correlation coefficient between the proportion of scintillation-affected satellites and the fixing rate is -0.9, indicating a strong negative correlation. In contrast, the left panel of Fig. 8 presents the results from 2019, a year of low solar activity. During this period, the fixing rate remaines consistently above 95%, while the proportion of scintillation-affected satellites stays entirely below 10%. The correlation coefficient between the two variables is only 0.01, suggesting an insignificant correlation.

The conventional NRTK user-end positioning method typically does not explicitly account for the impact of DD ionospheric interpolation residuals when constructing DD observation models. This simplification enables centimeter-level positioning accuracy during ionospheric quiet periods. However, during the periods of high solar activity, intense spatiotemporal gradients in ionospheric electron density lead to significantly amplifing residual ionospheric errors after double differencing, severely degrading high-precision positioning performance on user-end. As illustrated by the September 2024 Hong Kong CORS network data in the bottom-right panel of Fig. 6, the fixing rate of the conventional RTK method

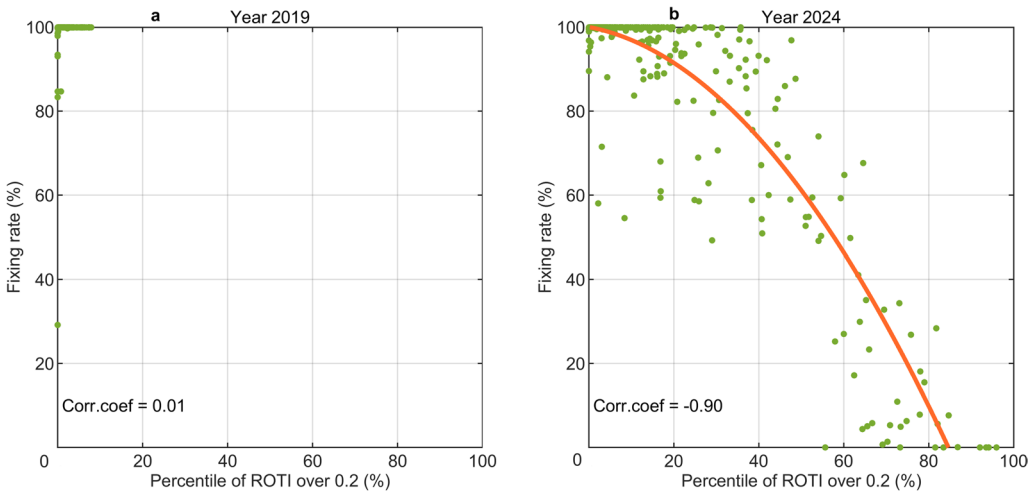

Fig. 8 Relationship between the proportion of ionospheric scintillation and fixing rate

notably decreases starting at GPS time 12:00. This phenomenon is closely linked to Equatorial Plasma Bubbles (EPBs) generated in the ionospheric F-region over the equatorial anomaly zone (Moreno et al., 2011; Gao et al., 2023; Li et al., 2024). EPBs, a classic form of ionospheric irregularities, exhibit strong vertical plasma density gradients that induce rapid GNSS phase fluctuations and severe amplitude scintillation, critically disrupting the spatial correlation of DD observations. To address these severe disturbance scenarios, this study employs Hong Kong CORS data in September 2024 to evaluate user-end positioning performance by incorporating ionospheric parameter estimation and an adaptive process noise methodology (Method A).

Figure 9 presents the fixing rate deviation between Method A and the conventional RTK method in September 2024. From the figure, the fixing rates show a significant improvement during most periods; however, performance degradation is observed in a minority of sessions. This study analyzed the fixing rate from GPS time 12:00 to 24:00 (spanning a 30-day period, every hour as a sample, totaling 360 samples). Among these samples, 88 cases show improvement while 10 cases exhibit degradation.

In severe ionospheric disturbance conditions, the ambiguity fixing rate of Method A is lower than that of the conventional RTK approach, primarily due to a significant reduction in the number of available satellites which is not scintillation-affected. Additionally, abnormal increases in ionospheric delay spatial gradients can cause ionospheric parameter estimation to fail with Method A. To mitigate these issues, this study further refines the stochastic observation model of Method A based on the proportion of ionospheric scintillation. Specifically, the satellites with scintillation-attecfted proportions exceeding 50% are excluded from the observation model. For the satellites with scintillation-attecfted proportions between 35 and 50% (corresponding to thresholds a = 35% and b = 50% in the ROTI-based stochastic model described in Eq. (23)), observation weightings are reduced according to the relationship between scintillation proportion and interpolation errors defined in Eqs. (23) and (24). This refined approach forms the basis of Method B.

Using the data from GPS time 12:00:00 to 13:00:00 on September 4, 2024 (DoY 248) as an example, Fig. 10 depicts the ionospheric scintillation proportion during this interval. The horizontal axis lists satellite PRNs in descending order by their average ROTI values, while the vertical axis represents the scintillation proportion of the remaining satellites after sequential exclusion. A three-tier classification scheme is applied: gray markers indicate the satellites excluded due to scintillation

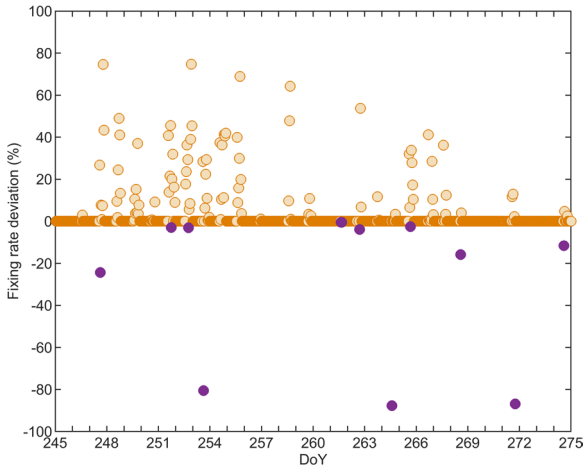

Fig. 9 User-end fixing rate difference of method A compared to conventional method in September 2024

proportions exceeding 50%, light yellow markers represent the satellites requiring weighting adjustments with scintillation proportions between 35 and 50%, and orange markers denote the satellites retaining their original weighting with proportions below 35%.

Figure 11 compares time-series positioning results with three methods under varying ionospheric scintillation conditions. Due to space limitations, one representative time period is selected for each ionospheric scintillation proportion range: 0–20%, 20–40%, 40–60%, and 60–80%. The figure displays positioning sequences in the East, North, and Up (ENU) directions obtained with the conventional RTK method, Method A, and Method

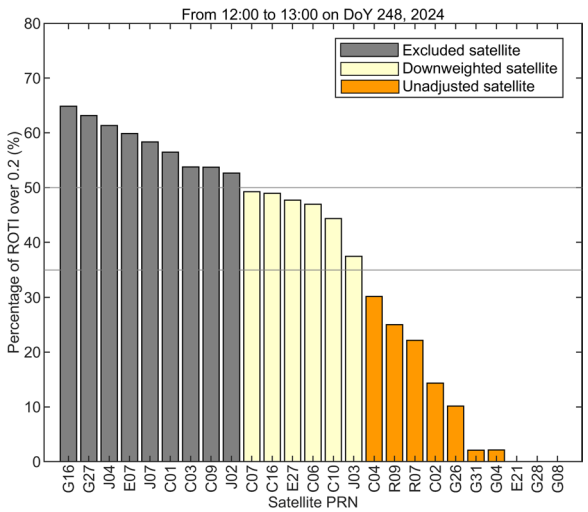

Fig. 10 The proportion of satellites affected by ionospheric scintillation and satellite weighting adjustment strategy of GPS hour 12–13 on September 4, 2024 (DoY 248)

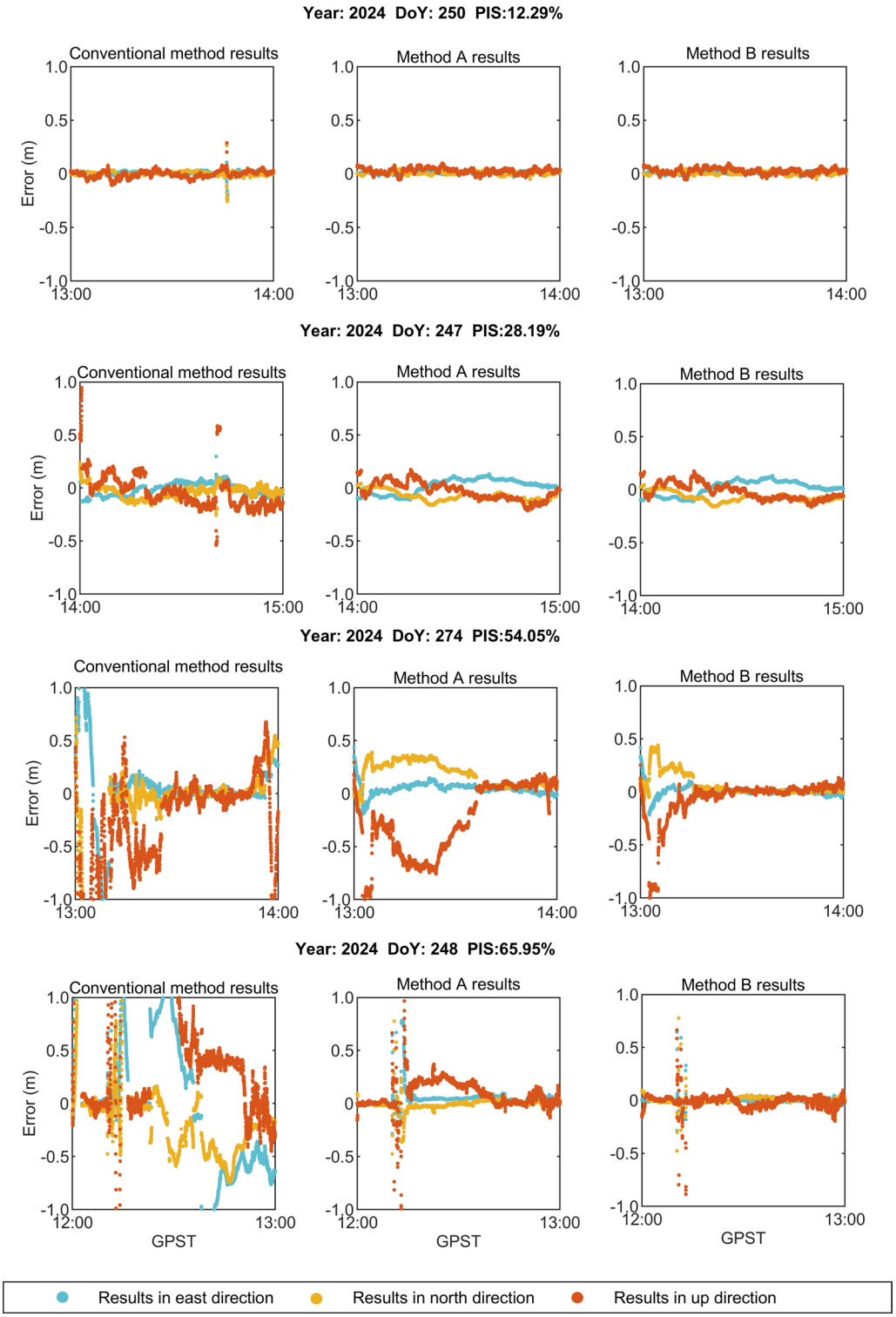

Fig. 11 User-end positioning errors with three methods for four periods

Table 2 Information of user-end fixing rate below 90% with conventional RTK method

No.	DoY	Hour	Fixing rate (%)	No.	DoY	Hour	Fixing rate (%)
1	254	17	0.00	45	264	12	54.78
2	258	13	0.00	46	274	14	54.83
3	258	16	0.00	47	254	21	58.06
4	262	13	0.00	48	254	19	58.58
5	262	14	0.00	49	266	16	58.86
6	262	15	0.00	50	248	17	58.89
7	255	14	0.03	51	253	17	59.00
8	255	16	0.03	52	251	13	59.28
9	255	15	0.08	53	254	20	59.44
10	247	18	0.72	54	254	12	59.50
11	254	16	1.39	55	249	18	60.06
12	269	15	1.39	56	252	20	60.97
13	274	12	4.39	57	247	14	62.83
14	258	15	4.97	58	251	15	64.86
15	267	13	5.06	59	267	12	67.17
16	252	17	5.33	60	265	13	67.64
17	268	12	5.64	61	251	19	68.06
18	249	15	5.81	62	247	13	68.94
19	249	16	6.33	63	252	14	69.08
20	262	16	7.64	64	253	18	70.69
21	258	14	7.83	65	266	21	71.53
22	254	13	10.92	66	265	17	72.11
23	255	17	15.56	67	249	12	74.00
24	268	13	17.22	68	248	15	75.56
25	249	17	18.14	69	255	18	79.56
26	248	12	23.36	70	251	18	79.61
27	258	12	25.25	71	252	13	82.22
28	252	21	25.28	72	265	18	82.69
29	262	12	26.89	73	248	13	82.92
30	265	16	27.03	74	251	21	83.75
31	253	12	28.39	75	248	18	85.42
32	254	18	29.94	76	251	14	85.97
33	252	15	32.86	77	271	14	87.06
34	252	16	34.39	78	267	17	87.61
35	253	13	35.08	79	251	22	88.11
36	262	17	41.08	80	259	18	88.19
37	274	13	49.14	81	263	17	88.36
38	247	19	49.25	82	271	13	88.36
39	251	16	49.83	83	253	19	89.00
40	247	17	50.31	84	249	14	89.42
41	248	16	50.94	85	254	15	89.53
42	255	13	52.69	86	265	19	89.53
43	251	17	54.33	87	266	22	89.58
44	252	22	54.56				

B during these four typical periods. The annotation "PIS" (Percentage of Ionospheric Scintillation) indicates the scintillation proportion without any satellite exclusion. At a scintillation proportion of 12.29%, all three methods achieve comparable positioning accuracy. When the scintillation proportion rises to 28.19%, both Method

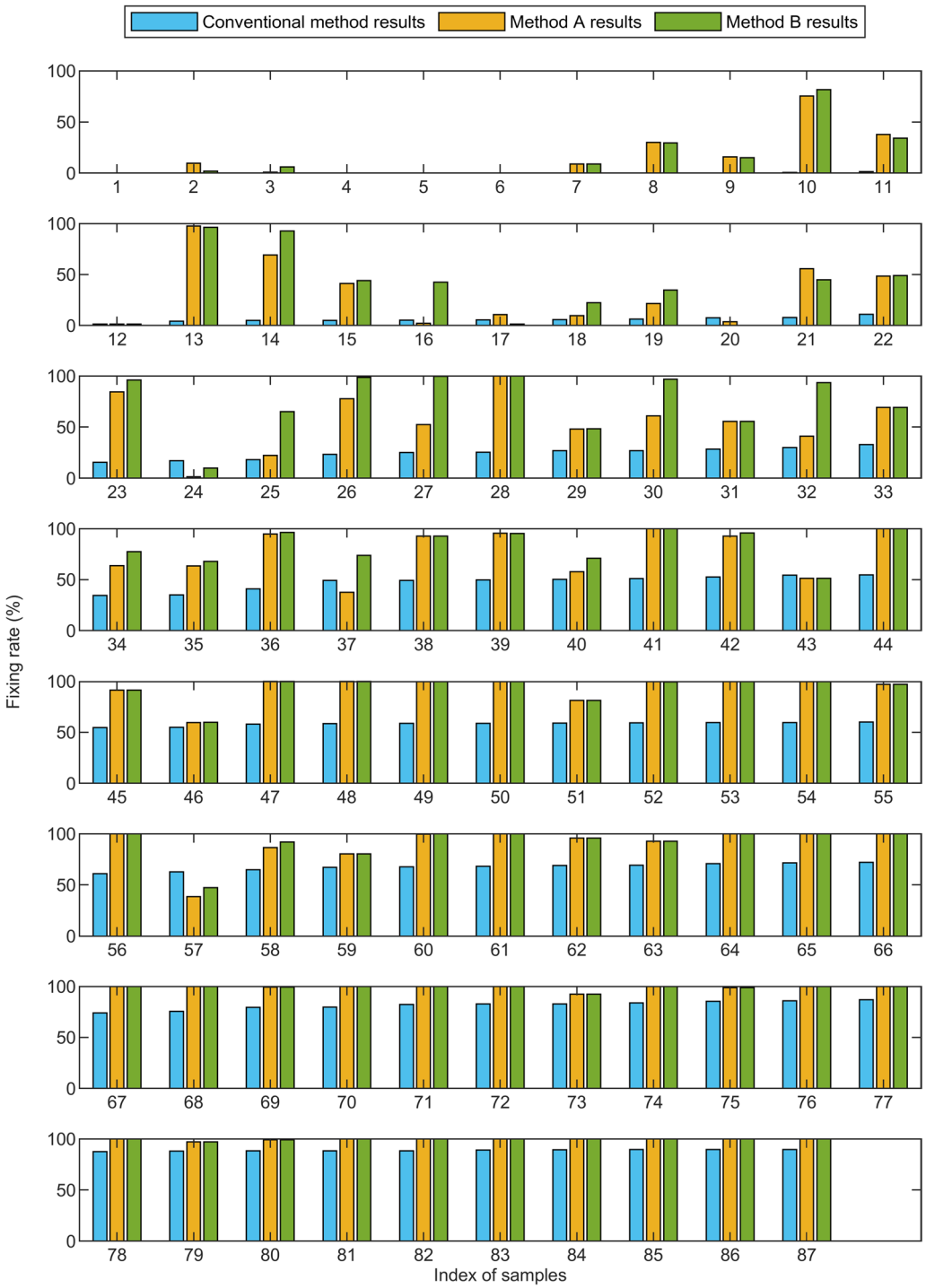

Fig. 12 User-end positioning fixing rate with three methods

A and Method B outperform the conventional method with similar performance. At higher scintillation levels of 54.05% and 65.95%, Method B shows significant improvement over Method A.

Table 2 lists the periods during which the user-end fixing rates of the conventional RTK method in NRTK fall below 90%, sorted in ascending order of fixing rate. Figure 12 presents a histogram comparing the fixing rates of the three methods for the 87 samples listed in Table 2.

Table 3 Availability improvement of methods A and B compared to conventional methods

Fixing rate range	Conventional method	Method A		Method B	
	No. of samples	No. of samples	Availability improvement (%)	No. of samples	Availability improvement (%)
0–30%	32	16	50	14	56
30–70%	31	19	39	14	55
70–90%	24	6	75	6	75
Sum	87	41	53	34	61

Table 4 Statistics of horizontal and vertical direction errors for three methods

Method	Horizontal RMS (cm)	Vertical RMS (cm)	Average fixing rate (%)
Conventional Method	6.93	12.76	58.6
Method A	5.42	8.49	79.8
Method B	4.32	7.45	84.1

The horizontal axis corresponds to the sample sequence numbers from Table 2, while the vertical axis indicates the fixing rates. The figure shows that most samples experience significant improvement in fixing rate when using Method A and Method B, with Method B consistently outperforming Method A.

Table 3 presents the distribution of user-end fixing rates for the 87 samples withr the three methods. With Method A, 46 out of 87 samples achieved fixing rates above 90%, corresponding to an availability of 53%. While Method B has 34 samples with fixing rates below 90% to 34 and 53 above 90% achieving a 61% improvement in availability.

Table 4 presents the RMS statistics of positioning errors for the 87 samples, excluding results with horizontal errors exceeding 50 cm and vertical errors exceeding 100 cm. The results indicate that the accuracy and average fixing rates of the three methods rank in descending order as Method B, Method A, and the conventional method.

Conclusions

Currently, solar activity has reached its peak within the 25th solar cycle, leading to a significant increase in ionospheric disturbances that adversely affect the accuracy and reliability of GNSS positioning. To address this issue, this study proposed a novel NRTK positioning method that integrates service-end disturbance information generation with user-end ionospheric residual estimation. By incorporating the ionospheric disturbance index ROTI along with an elevation-dependent weighting model, the stochastic model for user-end RTK positioning is further optimized to enhance adaptability in diverse ionospheric conditions. The data of the CORS network in the low-latitude region (HK, China) were employed to assess the performance of the proposed method. The main conclusions are summarized as follows:

(1) In years of high solar activity, the ionospheric disturbance index ROTI exhibits a strong positive correlation of 0.91 with the RMS of ionospheric interpolation errors. Conversely, in years of low solar activity, the RMS of ionospheric interpolation errors and the proportion of ROTI values exceeding 0.2 TECU/min are both low, resulting in a weak correlation coefficient of 0.11;
(2) During the periods of high solar activity, there is a significant negative correlation of −0.9 between ROTI and the NRTK user-end fixing rate. In contrast, in low solar activity years, the proportion of ROTI values above 0.2 remains small and fixing rates stay high, yielding a negligible correlation coefficient of 0.01;
(3) Statistical analysis of 360 hourly samples taken daily from 12:00 to 24:00 in September 2024 reveals that both Method A and Method B significantly improve RTK positioning availability compared to the conventional RTK method, with an improvement of 53% and 61%, respectively;
(4) Focusing on 87 samples where the fixing rate of the conventional RTK method was below 90%, Methods A and B demonstrated much higher fixing rates and positioning accuracy, with Method B the best performance. Compared to the conventional RTK method, the average fixing rate is increased from 58.6 to 79.8% for Method A and 84.1% for Method B. Horizontal positioning errors are decreased from 6.93 to 5.42 cm and 4.32 cm, reflecting improvement of 21.8% and 37.6%, respectively. Vertical positioning errors reduced from 12.76 to 8.49 cm and 7.45 cm, with improvements of 33.5% and 41.6%, respectively.

Acknowledgements
The authors are grateful for the use of GPS observation data provided by Hong Kong Geodetic Survey services (https://rinex.geodetic.gov.hk/rinex2/) and VTEC products provided by IGS (ftp://igs.gnsswhu.cn/pub/gps/products/ionex). The numerical calculations have been done on the supercomputing system in the Supercomputing Center of Wuhan University.

Author contributions
JSZ, XDR and XHZ conceived and defined the research theme. JSZ processed the data and wrote the manuscript. GFP and XDR discussed the methodological feasibility and provided data analysis. KJ carried out image processingng work. XDR, XHZ, YHY and AMEA revised the entire manuscript. All authors reviewed the manuscript.

Funding
This work was funded by the National Science Fund for Distinguished Young Scholars of China (Grant No. 42425003), the National Natural Science Foundation of China (Grant No. 42388102, No. 42230104) and the Fundamental Research Funds for the Central Universities (No. 2042025kf0026).

Data availability
Observation data from Hong Kong Geodetic Survey services (https://rinex.geodetic.gov.hk/rinex2/).The VTEC values from the IGS ionospheric grid files (ftp://igs.gnsswhu.cn/pub/gps/products/ionex).

Declarations

Competing interest
The authors declare no competing interests.

Received: 27 May 2025 Revised: 9 September 2025 Accepted: 9 September 2025
Published online: 06 October 2025

References

Al-Shaery, A. M., Lim, S., & Rizos, C. (2011). Investigation of different interpolation models used in network-RTK for the virtual reference station technique. *Journal of Global Positioning Systems, 10*(2), 136–148. https://doi.org/10.5081/jgps.10.2.136

Bae, T. S., & Kim, M. (2018). Performance analysis of network-RTK techniques for drone navigation considering ionospheric conditions. *Journal of Sensors, 2018*(1), 5154697. https://doi.org/10.1155/2018/5154697

Charoenkalunyuta, T., & Satirapod, C. (2014). Effect of Thai Ionospheric Maps (THIM) model on the performance of network based RTK GPS in Thailand. *Survey Review, 46*(334), 1–6.

Charoenkalunyuta, T., Satirapod, C., Lee, H. K., & Choi, Y. S. (2012). Performance of network-based RTK GPS in low-latitude region: A case study in Thailand. *Engineering Journal, 16*(5), 95–104. https://doi.org/10.4186/ej.2012.16.5.95

Cohen, J. (1988). *Statistical power analysis for the behavioral sciences* (2nd ed.). Routledge.

Cui, J., Tang, W., Jin, L., Deng, C., Zou, X., & Gu, S. (2018). An improved ionosphere interpolation algorithm for network RTK in low-latitude regions. *GPS Solutions, 22*, 1–11.

Dai, L., Han, S., Wang, J., & Rizos, C. (2003). Comparison of interpolation algorithms in network-based GPS techniques. *Navigation (Washington), 50*(4), 277–293. https://doi.org/10.1002/j.2161-4296.2003.tb00335.x

Dai, W., Shi, Q., & Cai, C. (2017). Characteristics of the BDS carrier phase multipath and its mitigation methods in relative positioning. *Sensors, 17*(4), 796.

Dobelis, D., Zvirgzds, J., & Kaļinka, M. (2017). High ionospheric activity effects on LatPos RTK network performance in Latvia. *IOP Conference Series: Materials Science and Engineering, 251*(1), 012064. https://doi.org/10.1088/1757-899X/251/1/012064

Dutta, U., Jarlemark, P., Rieck, C., & Johansson, J. (2022). Ionospheric Effects on GNSS RTK. In *Proceedings of the 35th International Technical Meeting of the Satellite Division of the Institute of Navigation*.

Follestad, A., Clausen, L., Moen, J. I., & Jacobsen, K. S. (2021). Latitudinal, diurnal, and seasonal variations in the accuracy of an RTK positioning system and its relationship with ionospheric irregularities. *Space Weather, 19*(6), Article e2020SW002625.

Fotopoulos, G., & Cannon, M. E. (2001). An overview of multiple-reference station methods for cm-level positioning. *GPS Solutions, 4*(3), 02–10.

Gao, Y., Li, Z. (1997). Carrier phase based regional area differential GPS for decimeter-level positioning and navigation. In *Proceeding of ION GNSS 1997, institute of navigation*, Nashville, Tennessee, USA, September 19–22, pp. 91–97.

Gao, Y., Li, Z. (1998). Ionosphere effect and modeling of regional area differential GPS network. Proceeding of ION GNSS 1998, institute of navigation, Nashville, Tennessee, USA, September 18–21, pp.91–97.

Gao, H., Zhang, D., Liu, Z., Sun, S., Hao, Y., & Xiao, Z. (2023). Revisiting the variation of the ionospheric irregularities in the low latitude region of China based on small regional geodetic GNSS station network. *Space Weather*. https://doi.org/10.1029/2023SW003452

Gao, R., Liu, Z., & Zhang, B. (2022). Ionosphere-weighted post-processing kinematic for airborne positioning with refined modeling of receiver phase biases and tropospheric zenith wet delays. *GPS Solutions, 26*(4), 113. https://doi.org/10.1007/s10291-022-01299-z

Gao, W., Zhang, Z., Pan, S., Liu, H., Tao, X., & Zhao, Q. (2025). An adaptive NRTK ionospheric regional modeling method integrating baseline neighborhood enhancement and weighted lower-order surface model. *Measurement*. https://doi.org/10.1016/j.measurement.2025.117653

Gao, W., Zhou, W., & Tang, C. (2024). High-precision services of BeiDou navigation satellite system (BDS): Current state, achievements, and future directions. *Satellite Navigation, 5*, Article 20. https://doi.org/10.1186/s43020-024-00143-8

Gao, X., Liu, J., & Ge, M. (2002). An ambiguity searching method for network RTK baselines between base stations at single epoch. *Acta Geodaetica Et Cartographica Sinica, 31*(4), 305–309. https://doi.org/10.3321/j.issn:1001-1595.2002.04.005

Gianniou, M., & Mitropoulou, E. (2012). Impact of high ionospheric activity on GPS surveying: Experiences from the Hellenic RTK-network during 2011–12. *EUREF Annual Symposium, 2012*, 6–8.

Gong, X.L. (2008). Research on construction of vast gps cors reference stations network, Ph.D. dissertation, Wuhan University, Wuhan, China (in Chinese).

Gu, S., Fang, L., & Jiang, W. (2024). Multiple integer candidates ambiguity resolution: A unification ambiguity resolution algorithm. *Satellite Navigation, 5*, Article 21. https://doi.org/10.1186/s43020-024-00141-w

Gu, S., Gan, C., & He, C. (2022). Quasi-4-dimension ionospheric modeling and its application in PPP. *Satellite Navigation, 3*, Article 24. https://doi.org/10.1186/s43020-022-00085-z

Han, S., Rizos, C. (1996). GPS network design and error mitigation for real-time continuous array monitoring systems. Proceeding of ION GNSS 1996, institute of navigation, Kansas city, Missouri, USA, September 17–20, pp. 1827–1836.

Han, S. (1997). Carrier Phase-Based Long-Range GPS Kinematics Positioning, Ph.D. dissertation, The University of New South Wales, Sydney, Australia.

Herbert, L., Vollath, U., & Chen, X. (2002). Virtual reference station systems. *Journal of Global Positioning Systems, 1*(2), 137–143.

Hofmann-Wellenhof, B., Lichtenegger, H., & Wasle, E. (2007). *GNSS–global navigation satellite systems: GPS, GLONASS, Galileo, and more*. Springer.

Jha, B. K., & Upton, L. A. (2024). Predicting the timing of the solar cycle 25 polar field reversal. *The Astrophysical Journal Letters, 962*(1), L15.

Jia, H., Yang, Z., & Li, B. (2024). ROTI-based statistical regression models for GNSS precise point positioning errors associated with ionospheric plasma irregularities. *GPS Solutions, 28*, 105. https://doi.org/10.1007/s10291-024-01648-0

Julien, O., Alves, P., & Cannon, M.E. (2004). Improved Triple-Frequency GPS/GALILEO carrier phase ambiguity resolution using a stochastic ionosphere modeling. In *Proceedings of the 2004 National Technical Meeting of The Institute of Navigation*. San Diego, CA, pp.441–452.

Li, C. (2007). Generation and distribution technique of precise differential corrections for GPS/VRS network, Ph.D. dissertation, Southwest Jitaotong University, Chengdu, China (in Chinese).

Li, B., Shen, Y., Feng, Y., Gao, W., & Yang, L. (2014). GNSS ambiguity resolution with controllable failure rate for long baseline network RTK. *Journal of Geodesy, 88*(2), 99–112.
Li, W., & Jiang, Y. (2024). Equatorial plasma bubble model and integrity risk evaluation for ground based augmentation system in Hong Kong. *Satellite Navigation, 5*, Article 32. https://doi.org/10.1186/s43020-024-00154-5
Liu, H., Zhang, Z., Sheng, C., Yu, B., Gao, W., & Meng, X. (2024). Fast and reliable network RTK positioning based on multi-frequency sequential ambiguity resolution under significant atmospheric biases. *Remote Sensing, 16*(13), 2320.
Liu, J., Tu, R., Han, J., Zhang, R., Fan, L., Zhang, P., Hong, J., & Lu, X. (2020). Initial evaluation and analysis of NRTK positioning performance with new BDS-3 signals. *Measurement Science and Technology, 32*(1), Article 014002.
Liu, K., Li, G., Ning, B., Hu, L., & Li, H. (2015). Statistical characteristics of low-latitude ionospheric scintillation over China. *Advances in Space Research, 55*(5), 1356–1365.
Luo N, Dao TD, Lachapelle G, & Cannon E. (2005). GPS Network RTK Performance under very active ionospheric conditions. In *Proceedings of the 18th International Technical Meeting of the Satellite Division of The Institute of Navigation (ION GNSS 2005)*, Long Beach, CA, USA, September 13–16, pp 2531–2539.
Mei, S.Q. (2008). Research on information service integration framework of multiple cors systems and its network construction technology, Ph.D. dissertation, Wuhan University, Wuhan, China (in Chinese).
Mi, X., Zhang, B., & Yuan, Y. (2019). Stochastic modeling of between-receiver single-differenced ionospheric delays and its application to medium baseline RTK positioning. *Measurement Science and Technology, 30*(9), 095008.
Mirmohammadian, F., Asgari, J., Verhagen, S., & Amiri-Simkooei, A. (2022). Multi-GNSS-weighted interpolated tropospheric delay to improve long-baseline RTK positioning. *Sensors, 22*(15), 5570.
Moreno, B., Radicella, S., Lacy, M., Herraiz, M., & Caderot, G. (2011). On the efects of the ionospheric disturbances on precise point positioning at equatorial latitudes. *GPS Solutions, 15*, 381–390. https://doi.org/10.1007/s10291-010-0197-1
Odijk D, Teunissen P. (2010). Improving the speed of CORS Network RTK ambiguity resolution. Position Location and Navigation Symposium, IEEE/ION, 79–84. https://doi.org/10.1109/PLANS.2010.5507203
Odijk, D., Marel, H., & Song, I. (2000). Precise GPS positioning by applying ionospheric corrections from active control networks. *GPS Solutions, 11*(3), 49–57.
Odolinski, R., & Teunissen, P. (2017). Low-cost, 4-system, precise GNSS positioning: A GPS, Galileo, BDS and QZSS ionosphere-weighted RTK analysis. *Measurement Science and Technology, 28*(12), Article 125801. https://doi.org/10.1088/1361-6501/aa92eb
Odolinski, R., & Teunissen, P. (2019). An assessment of smart phone and low-cost multi-GNSS single-frequency RTK positioning for low, medium and high ionospheric disturbance periods. *Journal of Geodesy, 93*(5), 701–722. https://doi.org/10.1007/s00190-018-1192-5
Paziewski, J. (2016). Study on desirable ionospheric corrections accuracy for network-RTK positioning and its impact on time-to-fix and probability of successful single-epoch ambiguity resolution. *Advances in Space Research, 57*(4), 1098–1111. https://doi.org/10.1016/j.asr.2015.12.024
Paziewski, J., Høeg, P., Sieradzki, R., Jin, Y., Jarmolowski, W., Hoque, M. M., Berdermann, J., Hernandez-Pajares, M., Wielgosz, P., Lyu, H., Miloch, W. J., & Perez, O. (2022). Theimplications of ionospheric disturbances for precise GNSS positioning in Greenland. *Journal of Space Weather and Space Climate*. https://doi.org/10.1051/swsc/2022029
Paziewski, J., & Sieradzki, R. (2020). Enhanced wide-area multi-GNSS RTK and rapid static positioning in the presence of ionospheric disturbances. *Earth, Planets and Space, 72*(1), 110. https://doi.org/10.1186/s40623-020-01238-7
Paziewski, J., & Wielgosz, P. (2014). Assessment of GPS + Galileo and multi-frequency Galileo single-epoch precise positioning with network corrections. *GPS Solutions, 18*(4), 571–579. https://doi.org/10.1007/s10291-013-0355-3
Peng, Y., Scales, W. A., & Hartinger, M. D. (2021). Characterization of multi-scale ionospheric irregularities using ground-based and space-based GNSS observations. *Satellite Navigation, 2*, Article 14. https://doi.org/10.1186/s43020-021-00047-x
Pereira, V., Monico, J., & Camargo, P. (2021). Detection of solar flare using IGS network stations: Case study for September 6, 2017. *Revista Brasileira De Geomatica, 9*(2), 103–119. https://doi.org/10.3895/rbgeo.v9n2.13418
Pi, X., Mannucci, A., Lindqwister, U., & Ho, C. (1997). Monitoring of global ionospheric irregularities using the worldwide GPS network. *Geophysical Research Letters, 24*(18), 2283–2286.
Raquet, J. (1998). Development of A method for kinematic GPS carrier phase ambiguity resolution using multiple reference receivers, Ph.D. dissertation, University of Calgary, Alberta, Canada.
Ren, X., Le, X., Mei, D., Liu, H., & Zhang, X. (2024). IROTI: a new index to detect and identify traveling ionospheric disturbances and equatorial plasma bubbles. *GPS Solutions, 28*(1), 7. https://doi.org/10.1007/s10291-023-01545-y
Rizos, C. (2009). Network RTK research and implementation: a geodetic perspective. *Positioning*, *1*(02).
Takasu T., Yasuda A. (2009). Development of the low-cost RTKGPS receiver with an open source program package RTKLIB. In *International Symposium on GPS/GNSS, International Convention Center Jeju*, Korea, November 4–6.
Tang, W., Jin, L., Cui, J., Shi, C., & Zhang, Y. (2016). GNSS network RTK regional ionospheric modelling studies and performance analysis. *The Journal of Navigation, 69*(01), 211–224. https://doi.org/10.1017/S0373463315000636
Teunissen, P. (1995). The least-squares ambiguity decorrelation adjustment: A method for fast GPS integer ambiguity estimation. *Journal of Geodesy, 70*(1–2), 65–82. https://doi.org/10.1007/BF00863419
Tominaga T, Kondo K, Kubo N, & Yasuda A. (2004). The Ionospheric Effect on MediumBaseline RTK-GPS Positioning. In *The 2004 International symposium on GNSS/GPS, Sydney, Australia*.
Vollath U., Landau H., Chen X., Doucet K., & Pagels C. (2002). Network RTK versus single base RTK-understanding the error characteristics. In *Proceedings ION GPS 2002, Institute of Navigation, Portland, Oregon, USA*, September 24–27, pp 2774–2781.
Wang, P., Nie, G., Liu, H., Wen, J., Wang, Y., & Shen, H. (2023). An ionosphere-weighted calibration method with multi-station network corrections. *Advances in Space Research, 72*(9), 3982–3997.
Wanninger, L. (1995). Enhancing differential GPS using regional ionospheric error models. *Bulletin Géodésique, 69*, 283–291.
Wanninger, L. (2004). Introduction to network RTK. *IAG Working Group, 4*(1), 2003–2007.
Weng, D., Ji, S., Lu, Y., Chen, W., & Li, Z. (2021). Improving DGNSS performance through the use of network RTK corrections. *Remote Sensing, 13*(9), 1621. https://doi.org/10.3390/rs13091621
Wielgosz, P. (2011). Quality assessment of GPS rapid static positioning with weighted ionospheric parameters in generalized least squares. *GPS Solutions, 15*(2), 89–99. https://doi.org/10.1007/s10291-010-0168-6
Wielgosz, P., Kashani, I., & Grejner-Brzezinska, D. (2005). Analysis of long-range network RTK during a severe ionospheric storm. *Journal of Geodesy, 79*(9), 524–531. https://doi.org/10.1007/s00190-005-0003-y
Wu, S. (2009). Performance of regional atmospheric error models for NRTK in GPSnet and the implementation of a NRTK system, Ph.D. dissertation, RMIT University, Melbourne, Australia.
Wübbena, G., Bagge, A., & Seeber, G. (1996). Reducing distance dependent errors for real-time precise DGPS applications by establishing reference station networks. In *Proceeding of ION GNSS 1996, institute of navigation*, Kansas city, Missouri, USA, September 17–20, pp. 1845–1852.
Yang, F., Meng, X., & Guo, J. (2021). Development and evaluation of the refined zenith tropospheric delay (ZTD) models. *Satellite Navigation, 2*, Article 21. https://doi.org/10.1186/s43020-021-00052-0
Zhang, J., Ren, X., Mei, D., Abdelaziz, A., Zhang, X., Pan, G., & Jiang, K. (2024). Long-term analysis of NRTK positioning performances over one solar activity cycle from 2013 to 2023. *GPS Solutions, 28*(4), 179. https://doi.org/10.1007/s10291-024-01727-2
Zhang, R., Gao, C., & Wang, Z. (2022). Ambiguity resolution for long baseline in a network with BDS-3 quad-frequency ionosphere-weighted model. *Remote Sensing*. https://doi.org/10.3390/rs14071654
Zhang, W., Zhang, J., Zuo, X., Li, H., Pan, G., & Wang, J. (2025). New data processing methods for network RTK positioning: Improving ionospheric uncertainty management during ionospheric scintillations. *GPS Solutions, 29*(2), Article 72.
Zhu, F., Chen, X., & Ma, L. (2023). S2L-RTK: Temporal ionospheric modeling for RTK baselines varying from short to long. *GPS Solutions, 27*, 156. https://doi.org/10.1007/s10291-023-01505-6

Zou, R., Liu, H., Yao, Y. B., & Shi, C. (2005). Application of delaunay triangulation network technology in continuous operation of satellite positioning service system. *Journal of Geomatics, 06*, 09–11 (in Chinese).

Publisher's Note